29th Symposium on Naval Hydrodynamics
Gothenburg, Sweden, 26-31 August 2012

High-Fidelity Curvilinear-Grid Two-Phase Flow Solvers for Ship Hydrodynamics

Jianming Yang, Zhaoyuan Wang,
Seongmo Yeon, Bonguk Koo, Frederick Stern
(IIHR-Hydroscience and Engineering, University of Iowa,
Iowa City, IA 52242, USA)

ABSTRACT

The oncoming exascale high-performance computing era is to revolutionize our approaches to grand scientific and engineering challenges. High-fidelity, first-principles-based simulations with unprecedented resolution can reveal vast unknown temporal-spatial correlations in multi-scale and multi-physics phenomena that are beyond today's computing capabilities. However, exascale platforms will be dramatically different from current mainstream supercomputers in terms of computing power and parallel architectures; and few codes could make full use of their potentials without major overhauls or even rewrite for minimized dependence on phenomenological/empirical models and substantially improved scalability. To meet the challenges of exascale computing for fundamental studies and simulation-based design in ship hydrodynamics, IIHR is developing the next-generation high fidelity solvers for real-world applications. In this paper, the development of a general structured grid two-phase solver is summarized. The focus is on improvements of orders of magnitude in accuracy, robustness, and performance for fully resolved, fully coupled, sharp-interface multi-phase turbulent ship flows utilizing billions of grid points. Some preliminary results are demonstrated for plunging breaking waves behind a bump using 2.2 billion grid points running on thousands of processors. This simulation has resolved for the first time and identified physics of the plunging wave breaking process, spray formation and wake spreading.

INTRODUCTION

Ship hydrodynamics presents many simulation challenges due to a wide variety of multi-phase, multi-physics, and multi-scale phenomena. For example, frequently encountered multi-phase phenomena are: air-water interface, bubbles, droplets, foam, saline, plume, etc, although single-phase water flows with or even without the free-surface boundaries are considered in many simplified cases. On the other hand, in many studies, multi-physics phenomena, such as fluid-structure interaction, waves, turbulence, cavitation, and acoustics, play the major role. As to multi-scale phenomena, some good examples are turbulence in the boundary layers and wakes, breaking waves under gravity and surface tension, etc. Because of the vast scales involved and the interactions of different scales between them, turbulence and phase interface phenomena pose the primary computational challenges. Moreover, fluid-structure interactions of the multiphase flow around a surface ship with various appendages and control surfaces further complicate the scenario.

Traditionally, potential flow solvers are used as the major tools in ship design. Unfortunately, the missing turbulence effects and limited free-surface capabilities restrict the applications of these solvers from work beyond the preliminary design stage, especially, for the modern non-conventional hull geometries and new propulsion concepts. Recently, due to the easy access to high-end desktops, non-expensive clusters and major supercomputers, various RANS solvers start to undertake and expand the simulation part in the ship design process. Milestone achievements such as dynamic overset grid technique (Carrica et al., 2007) have greatly accelerated the transition. However, as the high-performance computing community is advancing to the exa-scale (and beyond) computing era, the users of these solvers usually find their computations benefit from this computing revolution far less than expected in terms of better accuracy, shorter turnaround time, and larger scale cases. The major reasons are these solvers rely on a variety of simplified, phenomenological/empirical models designed for estimating the integral scales and different kinds of low-order, diffusive schemes for numerical stability consideration. These models and schemes were developed to accommodate computations with marginal spatial and temporal resolutions, which were typical scenario at

the time of very limited available computing resources. In addition, most of solvers were designed before the massively parallel computers from concepts became reality, thus lacks in conforming data structures and communication models that scale well on these modern parallel machines of tens/hundreds of thousands of computing cores. Due to these built-in limitations, it is not difficult to explain why the users cannot meet their expectations with the old solvers on the new platforms.

In view of the computational challenges we are facing and the non-optimum CFD tools we have in hand, new CFD solvers have to be developed to address these problems as much as possible from first principles and exploit sufficiently our current peta-scale and the oncoming exa-scale supercomputers. A new-generation high-fidelity ship hydrodynamics CFD toolbox (CFDShip-Iowa version 6) has been under development for the last few years at IIHR toward this direction. It is designed for the high-resolution, high-fidelity, multi-scale simulation of unsteady, multi-phase, multi-physics, turbulent flows in ship hydrodynamics utilizing billions of grid points and tens/hundreds of thousands of computing cores.

In the course of developing this high-fidelity ship hydrodynamics CFD toolbox, a series of choices have been made with regard to mathematical modeling approaches and numerical methods and related enabling technologies have been implemented, which gives our toolbox some unique advantages compared with other CFD solvers in terms of ship hydrodynamics related fundamental and applied studies. For instance, the realistic, fully-coupled, immiscible, two-phase flows are modeled by a single set of governing equations. Many solvers are limited to free-surface flows; and there are some solvers tackling the two-phase problems in a phase-by-phase manner with various simplified coupling conditions. Also, large-eddy simulation (LES) methodology is adopted as the major strategy for turbulence modeling using Lagrangian dynamic subgrid scale stress model. In addition, the air-water interface is treated in a sharp interface manner and tracked using a strongly conservative volume-of-fluid scheme. Many solvers use level set methods, which are well-known for not conserving mass in the course of interface evolution. For solvers using algebraic volume-of-fluid methods that advect a color function, the interface is usually diffused into a band of several grid cells. Usually sharp interface treatment is associated with level set methods, or hybrid level set methods such as particle level set, coupled level set and volume of fluid methods. In our solver, the distance function is constructed from the volume fraction function in the volume-of-fluid method and there is no level set advection procedure. With regard to other aspects of the numerical methods, our toolbox deals with time-accurate unsteady flow simulation using fractional-step method with second-order or third-order time advancement schemes. The SIMPLE family algorithms are not efficient for simulating unsteady flows as they were designed for steady flows. A staggered variable arrangement for exact projection is chosen for the velocity-pressure coupling procedure. The staggered, face-centered, contravariant velocity components are reconstructed from the cell-centered, Cartesian velocity components for great efficiency. Also, balanced force treatment for surface tension and gravity, which appear as singular forces in the pressure gradient terms. This treatment is critical for small-scale simulations. Several high-order advection schemes are available in our toolbox such as the third-order QUICK, and various WENO schemes of up to fifth-order accuracy, which are essential for the advection-dominant turbulent flows. On the contrary, many commercial solvers are still recommending first-order upwind scheme or use it as the default scheme. We've also developed unconditionally stable, high-order semi-Lagrangian advection schemes for momentum equations and VOF equations. While most of the solvers are still working on different implicit schemes through combinations of lower-order schemes and higher-order schemes through deferred correction, and fighting with numerical stability issues, our solver has been enjoying the highly successful semi-Lagrangian schemes prominent in the numerical weather prediction community. Particularly, we use a geometrical multigrid linear solver through the state of the art Hypre library, which is a highly scalable, very robust package capable of solving large-scale problems on hundreds of thousands of CPU cores.

To be specific, several milestone achievements have been accomplished in the last few years in an immersed boundary Cartesian grid solver for naval hydrodynamics, with regard to essential aspects such as interface modeling, turbulence modeling, six DOF motion capability, and high-performance computing, etc. On one hand, starting with a Lagrangian dynamic subgrid-scale (SGS) model for large-eddy simulations (LES) of low to moderate Reynolds number transitional and turbulent flows, several turbulence models were implemented in the solver, such as the one-equation Spalart-Allmaras and two-equation SST k-omega and k-g turbulence models with a wall function option. These RANS models together with the SGS models facilitate further work toward hybrid RANS/LES models for high Reynolds number flows. On the other hand, the high-fidelity ship hydrodynamics CFD toolbox uses a level-set based sharp interface method for liquid-gas interface treatment. Initially, high-order level set method (5th-order WENO and 3rd-order TVD RK schemes) was used for interface tracking (Yang &

Stern, 2009); then an improved hybrid particle level set method was developed for enhanced volume conservation properties (Wang et al., 2009a); later, an efficient coupled level-set and volume-of-fluid method was developed for robust and refined interface tracking (Wang et al., 2009b); recently, a novel volume-of-fluid method was achieved for general structured grids with a constructed level set function (Wang et al., 2012a). These contributions have greatly advanced our capabilities of accurately capturing small-scale interfacial phenomena as well as larger scale breaking or non-breaking waves. Significant improvements for HPC, such as three-dimensional domain decomposition, Hypre semi-coarsening multigrid Poisson solver, and parallel I/O using MPI2 were also accomplished a few years ago (Yang et al., 2008). Advances in other areas, such as semi-Lagrangian advection schemes for volume-of-fluid method and momentum equations (Wang et al., 2012b; Wang et al., 2012c), and a six DOF motion prediction algorithm (Yang & Stern, 2012), have been completed too.

In Suh et al. (2011) and Wang et al. (2012c), the Cartesian grid solver discussed above was extended into an orthogonal curvilinear solver with similar accuracy and efficiency, whereas resolving turbulent boundary layers and small droplets/bubbles at once. In terms of modeling, this solver has most components from the Cartesian grid solver except six DOF prediction capabilities using immersed boundary method. The RANS turbulence models have not been fully verified and validated yet. Numerical methods and HPC components are the same. It uses a recently developed novel volume-of-fluid method for general structured grids with a constructed level set function (Wang et al., 2012a), thus it can be used for detailed simulations of interfacial phenomena such as wave breaking and wave-body interactions with simple geometries like cylinder, sphere, wedge, foil, etc. The orthogonal curvilinear grid solver has been used for studying the high Reynolds number, high Froude number turbulent flow past an interface-piercing circular cylinder and a wedge-shaped bow. In addition, an overset grid solver was presented in Bhushan et al. (2011), which couples the Cartesain grid solver and the orthogonal curvilinear grid solver via overset grid package SUGGAR. It uses SGS models for turbulence modeling and level set method for interface tracking. For solving the pressure Poisson equation, it uses the PETSc library. It is used as a tool for experiencing many ideas such as oversetting grid and hybrid RANS/LES techniques. Currently, it is used for studying interface-piercing circular cylinder and Wigley hull.

Based on the Cartesian grid solver and the orthogonal curvilinear grid solver, a general multi-block structured grid solver is currently being developed. It will maintain and extend the higher-order advection and volume conservative interface tracking schemes, and enhanced capabilities of handling complex geometries in ship hydrodynamics. The development of the high-fidelity ship hydrodynamics CFD toolbox will be focused on this solver. Cartesian grids and orthogonal curvilinear grids will be options and components available in this general solver for wider user choices and better efficiency for cases these components are applicable.

The focus of this paper will be on some recent work on the development and applications of the orthogonal curvilinear grid and general structured grid solvers.

MATHEMATICAL FORMULATION

For simplicity, vector notation will be used for all equations without regard to the coordinate systems in the following sections unless stated otherwise. The governing equations and discretizations for orthogonal curvilinear coordinates were given in Wang et al. (2012c).

Navier-Stokes Equations

Incompressible viscous flows of two immiscible fluids, e.g., air and water, are governed by the Navier-Stokes equations:

$$\frac{\partial \mathbf{u}}{\partial t} + \mathbf{u} \cdot \nabla \mathbf{u} = \frac{1}{\rho} \nabla \cdot (-p\mathbf{I} + \mathbf{T}) + \mathbf{g}, \tag{1}$$

$$\nabla \cdot \mathbf{u} = 0, \tag{2}$$

where t is the time, $\mathbf{u}$ is the velocity vector, p is the pressure, $\mathbf{I}$ is the unit diagonal tensor, ρ is the density, $\mathbf{g}$ represents the gravity acceleration, and $\mathbf{T}$ is the viscous stress tensor defined as

$$\mathbf{T} = 2\mu\mathbf{S}, \tag{3}$$

with μ the dynamic viscosity and $\mathbf{S}$ the strain rate

$$\mathbf{S} = \frac{1}{2}[\nabla \mathbf{u} + (\nabla \mathbf{u})^T]. \tag{4}$$

Interface Modeling

Interface Tracking

In the volume-of-fluid method, the VOF function, F, is defined as the liquid volume fraction in a cell with its value in between zero and one in a surface cell and zero and one in air and liquid, respectively. The advection equation of F is

$$\frac{\partial F}{\partial t} + \mathbf{u} \cdot \nabla F = 0. \tag{5}$$

We can also define the interface Γ as the zero level set of a signed distance function, ϕ, or the level set

function. The position of the interface can be reconstructed from the VOF function.

Interface Jump Conditions

Since the fluids considered here are viscous and no phase change occurs, the velocity across the interface Γ is continuous:

$$[\mathbf{u}] = 0, \tag{6}$$

where [ ] denotes the jump at the interface, i.e., $f_L^I - f_G^I$ for a variable f with superscript I representing interface and subscripts G and L denote gas and liquid, respectively. The exact jump condition for stress is

$$[\mathbf{n} \cdot (-p\mathbf{I} + \mathbf{T}) \cdot \mathbf{n}] = \sigma\kappa, \tag{7}$$

where $\mathbf{n}$ is the unit vector normal to the interface, σ is the coefficient of surface tension, and κ is the local curvature of the interface. With a smoothed viscosity and continuous velocity field, the stress jump condition reduces to

$$[p] = p_L^I - p_G^I = \sigma\kappa, \tag{8}$$

Large-Eddy Simulation

In the LES approach, the Navier-Stokes equations are spatially filtered such that the large, energy carrying eddies are resolved and the small scale, dissipative eddies are modeled by a sub-grid scale stress model. After applying the filter operation to Eqs. (1-2), we have

$$\frac{\partial \bar{\mathbf{u}}}{\partial t} + \bar{\mathbf{u}} \cdot \nabla \bar{\mathbf{u}} = -\frac{1}{\rho}\nabla \cdot \bar{p} - \nabla \cdot \bar{\boldsymbol{\tau}} + \frac{1}{\rho}\nabla \cdot [\mu(\nabla \bar{\mathbf{u}} + (\nabla \bar{\mathbf{u}})^{\mathrm{T}})] + \mathbf{g} \tag{9}$$

$$\nabla \cdot \bar{\mathbf{u}} = 0, \tag{10}$$

where $\bar{f}$ denotes the filter operation on a variable f, $\bar{\boldsymbol{\tau}} = \overline{\mathbf{u}\mathbf{u}} - \bar{\mathbf{u}}\bar{\mathbf{u}}$ is the subgrid-scale (SGS) stress tensor, whose deviatoric part is parametrized following the Smagorinsky procedure as:

$$\bar{\boldsymbol{\tau}} - \frac{1}{3}\mathrm{trace}(\bar{\boldsymbol{\tau}})\mathbf{I} = -2\nu_t \bar{\mathbf{S}}, \tag{11}$$

and the turbulent eddy viscosity is defined as

$$\nu_t = C\Delta^2 |\bar{\mathbf{S}}|, \tag{12}$$

with

$$|\bar{\mathbf{S}}| = \sqrt{2\bar{\mathbf{S}} \cdot \bar{\mathbf{S}}}. \tag{13}$$

The model parameter C in the eddy viscosity definition has to be determined to close the equations. In this paper the Lagrangian dynamic SGS model (Meneveau et al., 1996) is chosen as it can handle complex geometries without the requirement of homogeneous direction(s). Therefore, Eq. (2.10) can be rewritten in the following form

$$\frac{\partial \bar{\mathbf{u}}}{\partial t} + \bar{\mathbf{u}} \cdot \nabla \bar{\mathbf{u}} = -\frac{1}{\rho}\nabla \cdot \bar{p} + \nabla \cdot [\nu_t(\nabla \bar{\mathbf{u}} + (\nabla \bar{\mathbf{u}})^{\mathrm{T}})] + \frac{1}{\rho}\nabla \cdot [\mu(\nabla \bar{\mathbf{u}} + (\nabla \bar{\mathbf{u}})^{\mathrm{T}})] + \mathbf{g} \tag{14}$$

with the trace of subgrid-scale stress tensor $\frac{1}{3}\mathrm{trace}(\bar{\boldsymbol{\tau}})$ incorporated into $\bar{p}$.

NUMERICAL METHODS

Grids and Variable Arrangement

As discussed in the previous section, ship hydrodynamics involves many multi-phase, multi-scale, and multi-physics phenomena. And quality grids are very important to resolve these phenomena. In general, structured grids can provide the highest accuracy when carefully designed. Also, various numerical schemes have been developed for structured grids. On the other hand, structured grid generation requires a lot of human inputs and usually is the most time-consuming part in a simulation in terms of human hours. Unstructured grid generation can be mostly automated. Major problems with high-fidelity simulations of ship hydrodynamics applications using unstructured grids are the lack of mature higher-order advection schemes, accurate interface tracking and modeling algorithms, and efficient grid deformation/regeneration/oversetting methods, among others, on unstructured grids. High-order schemes represented by the discontinuous Galerkin method are promising for unstructured grids, but there are still many topics to be explored in order to apply them to the problems we are dealing with. In addition, at IIHR invaluable knowledge and experience have been gained in the course of development and applications of earlier versions of ship hydrodynamics CFD toolbox using structured grids. Structured grids, combined with oversetting techniques and local grid refinement, have been proven to be very cost-effective for ship hydrodynamics applications.

In this study, the orthogonal curvilinear grid solver and the general structured grid solver are discussed. The former requires orthogonal curvilinear grids and the latter can be applied to general structured grids. On orthogonal grids, contravariant velocity components defined on the cell face centers are used, and all other dependent variables are defined on the cell centers. For details, see Wang et al. (2012c).

The methods of general structured grid solvers differ in the choice of dependent variables and grid layout (non-staggered and staggered). Figure 1 shows various grid layouts and dependent variables. Non-staggered grid method is less complicated, but has a pressure-velocity decoupling problem. The dependent variables can be naturally coupled using the staggered grid method. The choice of the dependent variables

significantly affects the accuracy, efficiency, stability, and coding complexity of the staggered grid method (Shyy and Vu, 1991; Zang et al., 1994; He et al., 1996; Wesseling et al., 1999; Smith et al., 1993; Ge and Sotiropoulos, 2007). Contravariant velocity components are straightforward, and the advantages of staggered grid can be fully retained; but it involves complicated discretization and second-order derivatives of the metrics, which reduces the accuracy on non-smooth mesh. The discretization of the equations is relatively simple using the Cartesian velocity components and Christoffel symbols can be avoided with increased accuracy; but it is computationally expensive since nine momentum equations need to be solved for per computational cell (Zang et al., 1994).

For staggered grid layout as shown in Figs. 1a, b and c, the pressure is located at the cell center and the velocity components are defined at the cell face centers. The discretized continuity equation requires the volume fluxes at all face centers of the computational cell. For partially transformed case as shown in Fig. 1a, three Cartesian velocity components are defined at each face center where three momentum equations should be solved. This will triple the computational cost of the Cartesian coordinate, which is especially expensive for 3D simulations (Ge and Sotiropoulos, 2007). If only one Cartesian velocity component is defined at each face center as shown in Fig. 1b, the computational cost will be comparable to the Cartesian mesh (Shyy and Vu, 1991), but pressure-velocity decoupling problem may occur (Smith et al., 1993) and it is not suitable for flows with arbitrarily complex geometries. These difficulties associated with the partial transformation on staggered grid can be alleviated by using the Contravariant velocity components as shown in Fig. 1c. However, the discretization of the fully transformed equations is very complex and involves the Christoffel symbols of the second kind. The accuracy of the whole numerical method will be very sensitive to the grid smoothness since the second order derivatives of the metrics are needed.

Interface Modeling

Interface Tracking

The sharp interface method is used for the interface modeling based on a novel VOF method (Wang et al., 2012a) with constructed distance function on general structured grids. The interface is tracked using the VOF function by solving the advection equation,

$$\frac{\partial F}{\partial t} + V^i \frac{\partial F}{\partial \xi^i} = 0, \tag{15}$$

where V^i is the volume flux defined at the cell face of the i grid direction, i.e., ξ^i. The interface is reconstructed via the PLIC method and advected with a Lagrangian scheme. The distance functions (level set function) which are needed for the sharp interface treatment can be obtained directly from the reconstructed interface based on the VOF method. The advection equations for the distance functions are not needed. Without solving the level set advection and reinitialization equations, approximately 60% total CPU time for interface tracking can be saved. Geometrical properties, normal and curvature, are calculated from the constructed distance function. For details of the interface tracking algorithm using VOF function and level set reconstruction procedure, see Wang et al. (2012a).

Physical Properties

The effective density and viscosity at each grid point can be evaluated using the VOF function as,

$$\begin{aligned} \rho &= \rho_G(1-F) + \rho_L F \\ \mu &= \mu_G(1-F) + \mu_L F. \end{aligned} \tag{16}$$

The density and viscosity are only smeared in the interfacial cells. One of the advantages of this treatment is that the estimation of density and viscosity at the interfacial cells is more accurate and also benefits mass conservation.

With the distance function defined, the fluid properties, such as density and viscosity, are given by the following equations:

$$\begin{aligned} \rho &= \rho_G + (\rho_L - \rho_G)H(\phi) \\ \mu &= \mu_G + (\mu_L - \mu_G)H_\varepsilon(\phi). \end{aligned} \tag{17}$$

In the present study, the density keeps a sharp jump, whereas the viscosity is smoothed over a transition region across the interface using the smoothed Heaviside function same as in the immersed boundary Cartesian grid solver and the orthogonal curvilinear grid solver. The Heaviside function is given by

$$H(\phi) = \begin{cases} 1 & \text{if } \phi \geq 0 \\ 0 & \text{if } \phi < 0 \end{cases}, \tag{18}$$

and the smoothed Heaviside function is

$$H_\varepsilon(\phi) = \begin{cases} 1 & \text{if } \phi > \varepsilon \\ \frac{1}{2}\left[1 + \frac{\phi}{\varepsilon} + \frac{1}{\pi}\sin\left(\frac{\pi\phi}{\varepsilon}\right)\right] & \text{if } |\phi| \leq \varepsilon. \\ 0 & \text{if } \phi < -\varepsilon \end{cases} \tag{19}$$

Orthogonal Curvilinear Grid Solver

The orthogonal curvilinear grid solver (Suh et al., 2011, Wang et al., 2012c) is extended from the immersed boundary Cartesian grid solver (Yang and Stern, 2009) for two-phase incompressible viscous flows. A finite-difference method is used to discretize the governing equations on a non-uniform staggered orthogonal grid. Time advancement of the present study is based on the semi-implicit four-step fractional

step method. The diagonal diffusion terms are advanced with the second-order Crank–Nicholson method and the other terms by the second-order explicit Adams–Bashforth method. The pressure Poisson equation is solved to enforce the continuity equation. The convective terms are discretized using the fifth-order HJ-WENO scheme. The other terms are discretized by the second-order central difference scheme.

The initial interface tracking scheme in this solver (Suh, et al., 2011) was high-order level set method. Recently a second-order volume-of-fluid method (Wang et al., 2012a) for general structured grids with a constructed distance function was developed and implemented in this solver. This scheme can substantially improve the mass conservative property of the interface tracking capabilities. In addition, a semi-Lagrangian advection scheme was achieved and implemented in this solver (Wang et al., 2012c). Time steps much larger than what could be used with the semi-implicit scheme are possible now, which dramatically accelerate the overall computations.

Currently, non-inertial reference frame capability has been added to the solver for the studies of interface-piercing circular cylinder with a pure sway motion. The capability is implemented through a fictitious force added to the momentum equation to account for the effects of converting from the inertial reference frame fixed to the earth to the non-inertial reference frame fixed to the moving body. Although limited to a single object undergoing a rigid body motion, this enhancement can be very useful for many applications such as the above-mentioned one and water impact problems.

General Structured Grid Solver

In this solver, the Cartesian form Navier-Stokes equations will be solved on a general curvilinear grid using finite-volume methods. The dependent variables and grid layout is shown in Fig. 1d, where the contravariant fluxes are defined at the cell faces and the Cartesian velocity components are located at the cell centers. The contravariant fluxes at the centers of the cell faces are chosen as the dependent variables while the Cartesian velocity components at the cell centers are used as the auxiliary variables for the direct discretization of the convection and diffusion terms at cell centers. Contravariant fluxes of the convective and viscous terms at the cell faces can be interpolated from the cell-centered values. The numerical method developed in (Sussman et al., 2007) for the sharp interface two-phase flows on Cartesian grid will be used in the present study.

Time Discretization

A semi-implicit time-advancement scheme is adopted to integrate the momentum equations with the second-order Crank-Nicolson scheme for the diagonal viscous terms and the second-order Adams-Bashforth scheme for the convective terms and other viscous terms. A four-step fractional-step method (Choi and Moin, 1994) is employed for velocity-pressure coupling, in which a pressure Poisson equation is solved to enforce the continuity equation. The discretized equations are

$$\frac{\hat{u}_i-u_i^n}{\Delta t}=-\frac{1}{\rho}\frac{\partial p^n}{\partial x_i}-\left(\frac{3}{2}\frac{\partial u_i^n u_j^n}{\partial x_i}-\frac{1}{2}\frac{\partial u_i^{n-1}u_j^{n-1}}{\partial x_i}\right)+\frac{1}{2}\frac{1}{\rho}\frac{\partial}{\partial x_j}\left(\mu\frac{\partial \hat{u}_i}{\partial x_j}+\mu\frac{\partial u_i^n}{\partial x_j}\right)+\frac{1}{\rho}\frac{\partial}{\partial x_j}\left(\frac{3\mu}{2}\frac{\partial u_j^n}{\partial x_i}-\frac{\mu}{2}\frac{\partial u_j^{n-1}}{\partial x_i}\right)+g_i, \quad (18)$$

$$\frac{u_i^*-\hat{u}_i}{\Delta t}=\frac{1}{\rho}\frac{\partial p^n}{\partial x_i}, \quad (19)$$

$$\frac{\partial}{\partial x_j}\left(\frac{1}{\rho}\frac{\partial p^{n+1}}{\partial x_j}\right)=\frac{1}{\Delta t}\frac{\partial u_j^*}{\partial x_j}, \quad (20)$$

$$\frac{u_i^{n+1}-u_i^*}{\Delta t}=-\frac{1}{\rho}\frac{\partial p^{n+1}}{\partial x_i}, \quad (21)$$

where superscript n denotes time step, $\hat{u}_i$ and u_i^* are the first and second intermediate cell-centered velocities, respectively, and Δt is the time step. Integrating the nonlinear momentum equation over a computational cell of volume Ω yields,

$$\int\frac{\hat{u}_i-u_i^n}{\Delta t}d\Omega=\int\left[-\frac{1}{\rho}\frac{\partial p^n}{\partial x_i}-\left(\frac{3}{2}\frac{\partial u_i^n u_j^n}{\partial x_i}-\frac{1}{2}\frac{\partial u_i^{n-1}u_j^{n-1}}{\partial x_i}\right)+\frac{1}{2}\frac{1}{\rho}\frac{\partial}{\partial x_j}\left(\mu\frac{\partial \hat{u}_i}{\partial x_j}+\mu\frac{\partial u_i^n}{\partial x_j}\right)+\frac{1}{\rho}\frac{\partial}{\partial x_j}\left(\frac{3\mu}{2}\frac{\partial u_j^n}{\partial x_i}-\frac{\mu}{2}\frac{\partial u_j^{n-1}}{\partial x_i}\right)+g_i\right]d\Omega, \quad (22)$$

The above equation can be rewritten by applying the divergence theorem as,

$$\int\frac{\hat{u}_i-u_i^n}{\Delta t}d\Omega=-\frac{1}{\rho}\int p^n n_i dS-\frac{1}{2}\int\left(3u_i^n u_j^n-u_i^{n-1}u_j^{n-1}\right)n_j dS+\frac{1}{2}\frac{1}{\rho}\int\left(\mu\frac{\partial \hat{u}_i}{\partial x_j}+\mu\frac{\partial u_i^n}{\partial x_j}\right)n_j dS+\frac{1}{2}\frac{1}{\rho}\int\left(3\mu\frac{\partial u_j^n}{\partial x_i}-\mu\frac{\partial u_j^{n-1}}{\partial x_i}\right)n_j dS+\int g_i\, d\Omega, \quad (23)$$

where **n** are the outward normal to the cell faces.

The volume and surface integrals can be numerically approximated with summation over all the faces of a computational cell as

$$\frac{\hat{u}_i-u_i^n}{\Delta t}\Omega=-\frac{1}{\rho}\sum_{k=1}^{dim}\left[p^n n_i S\right]_{lf}^{uf}-\frac{1}{2}\sum_{k=1}^{dim}\left[\left(3u_i^n u_j^n-u_i^{n-1}u_j^{n-1}\right)n_j S\right]_{lf}^{uf}$$

$$+\frac{1}{2}\frac{1}{\rho}\sum_{k=1}^{dim}\left[\left(\mu\frac{\partial\hat{u}_i}{\partial x_j}+\mu\frac{\partial u_i^n}{\partial x_j}\right)n_jS\right]_{lf}^{uf}$$
$$+\frac{1}{2}\frac{1}{\rho}\sum_{k=1}^{dim}\left[\left(3\mu\frac{\partial u_j^n}{\partial x_i}-\mu\frac{\partial u_j^{n-1}}{\partial x_i}\right)n_jS\right]_{lf}^{uf}+g_i\,\Omega, \quad (24)$$

where k is the grid index of the cell faces, dim is the dimensions of the problem, lf means lower cell face and uf means upper cell face, S is the face area, and Ω is the cell volume.

Rearrange Eq. (24) it obtains

$$\hat{u}_i-\frac{\Delta t}{2\Omega}\frac{1}{\rho}\sum_{k=1}^{dim}\left[\mu\frac{\partial\hat{u}_i}{\partial x_j}n_jS\right]_{lf}^{uf}=u_i^n-\frac{\Delta t}{\Omega}\frac{1}{\rho}\sum_{k=1}^{dim}[p^n n_iS]_{lf}^{uf}-\frac{\Delta t}{2\Omega}\sum_{k=1}^{dim}[3U_k^n u_i^n-U_k^{n-1}u_i^{n-1}]_{lf}^{uf}+\frac{\Delta t}{2\Omega}\frac{1}{\rho}\sum_{k=1}^{dim}\left[\mu\frac{\partial u_i^n}{\partial x_j}n_jS\right]_{lf}^{uf}+\frac{\Delta t}{2\Omega}\frac{1}{\rho}\sum_{k=1}^{dim}\left[\left(3\mu\frac{\partial u_j^n}{\partial x_i}-\mu\frac{\partial u_j^{n-1}}{\partial x_i}\right)n_jS\right]_{lf}^{uf}+\Delta t g_i, \quad (25)$$

where U_k is volume flux normal to the cell face. With general structured grids this equation gives a 19-point stencil, which results in a very large linear system that is very expensive to solve. Usually for quality structured grids, the off-diagonal viscous terms are also treated explicitly. And Eq. (25) can be rewritten as,

$$\left(I-\frac{\Delta t}{2\Omega}D_I\right)\hat{u}_i=u_i^n-\frac{\Delta t}{\Omega}G(p^n)-\frac{3\Delta t}{2\Omega}[C(u_i^n)+D_E(u_i^n)]-\frac{\Delta t}{2\Omega}[C(u_i^{n-1})+D_E(u_i^{n-1})]+\frac{\Delta t}{2\Omega}D_I(u_i^n)+\Delta t g_i, \quad (26)$$

where

$$C(u_i)=\sum_{k=1}^{dim}[U_k u_i]_{lf}^{uf}, \quad (27)$$

$$D_I(u_i)=\frac{1}{\rho}\sum_{k=1}^{dim}\left[\mu\frac{\partial u_i}{\partial n_k}S\right]_{lf}^{uf}, \quad (28)$$

$$D_E(u_i)=\frac{1}{\rho}\sum_{k=1}^{dim}\left[\mu\frac{\partial u_i}{\partial n_{j,j\neq k}}S+\mu\frac{\partial u_j}{\partial x_i}n_jS\right]_{lf}^{uf}, \quad (29)$$

$$G(p)=\frac{1}{\rho}\sum_{k=1}^{dim}[pn_iS]_{lf}^{uf}, \quad (30)$$

I is the identity matrix; C represents the convection terms; D_I and D_E denote the diagonal and all the other viscous terms treated implicitly by the Crank-Nicolson and explicitly by the Adams-Bashforth scheme, respectively; G is for pressure terms.

Equation (26) can be approximated with the approximate factorization method as

$$\left(I-\frac{\Delta t}{2\Omega}D_{I1}\right)\left(I-\frac{\Delta t}{2\Omega}D_{I2}\right)\left(I-\frac{\Delta t}{2\Omega}D_{I3}\right)\hat{u}_i=u_i^n-\frac{\Delta t}{\Omega}G(p^n)-\frac{3\Delta t}{2\Omega}[C(u_i^n)+D_E(u_i^n)]-\frac{\Delta t}{2\Omega}[C(u_i^{n-1})+D_E(u_i^{n-1})]+\frac{\Delta t}{2\Omega}D_I(u_i^n)+\Delta t g_i, \quad (31)$$

The resulting tridiagonal linear equations are solved with a parallel tridiagonal system solver.

Spatial Discretization

In this solver, Cartesian velocity components, pressure, and other scalars are defined at the cell centers. A generic transport equation contains the time rate of change, convection, diffusion, and the source term can be applied to governing equations and will be solved in a general form. This approach can greatly increase the function reusability, algorithm extendibility, code readability, and code robustness.

Advection Terms High Reynolds number flows are advection dominated except in the boundary layers. Therefore, in simulating these flows the accuracy of the advection schemes usually determines the overall accuracy of the solver. In the immersed boundary Cartesian grid solver and the orthogonal curvilinear grid solver, we have successfully applied high-order advection schemes, particularly WENO, in highly complicated two-phase flow simulations. We also implemented an OIFS (operator-integration-factor splitting) scheme for the high-order semi-Lagrangian treatment of the advection terms. One of the major advantages of this scheme is very simple to implement in the framework of the original Eulerian advection schemes. But it is relatively expensive in terms of computational cost due to the introducing of many substeps. Recently, there is renewed interest in developing high-order, conservative semi-Lagrangian advection schemes. Compared to the Eulerian schemes, semi-Lagrangian schemes can achieve very large time steps without resorting to implicit treatment of the advection terms, which is very computationally expensive and complicated in implementation. Also, these shortcomings become exacerbated for local grid refinement, whereas semi-Lagrangian schemes can be fitted in very nicely.

For orthogonal or nearly orthogonal grids, all advection schemes implemented in orthogonal grid solvers can be applied directly. The current implementation of semi-Lagrangian schemes is based on Strang splitting technique, and the three-dimensional case is just a combination of three one-dimensional advection operations. We've also developed a Strang splitting semi-Lagrangian advect scheme for the volume-of-fluid method on Cartesian grids, which can better conserve mass than the current Eulerian shcemes and can use CFL numbers of one order of magnitude of the Eulerian schemes. In the current solver, this VOF

advection scheme will be extended to curvilinear grids and the accuracy will be verified. Also, some high-order conservative semi-Lagrangian schemes based on ENO and WENO reconstruction techniques developed by Prof. Chi-Wang Shu and his co-workers will be extended to curvilinear grids and two-phase flows. Currently, we are working on literature survey to evaluate various schemes in terms of their accuracy and complexity and the possibility of their extensions to curvilinear grids and two-phase flows.

On distorted grids, evaluation of fluxes using only points along a grid line becomes less accurate even when one-dimensional high-order schemes are applied. Multi-dimensional reconstruction stencils have to be used to correctly evaluate the face fluxes. When combined with semi-Lagrangian schemes, the procedure will bear some similarity with the unstructured grid methods and a lot of geometric operations will be involved.

Implementation of advection schemes for distorted grids in the general structured grid soler will be started with a second-order central difference scheme. Then second-order and higher-order upwind schemes will be implemented. Eventually high-order semi-Lagrangian schemes will be implemented in order to run high-fidelity simulations with large time steps on general structured grids.

The face normal volume flux U_k can be evaluated from the neighboring cell-center values as follows,

$$U_k = \left(u_j n_j S\right)_k, \tag{32}$$

with the Cartesian velocity components, $\left(u_j\right)_k$, at the cell faces approximated by

$$\left(u_j\right)_k = \frac{(u_j)_c + (u_j)_{nbr}}{2}, \tag{33}$$

where c and nbr are the indices of the cell considered and its neighboring cell in the k grid direction.

Diffusion and Source Terms Diffusion and source terms will be discretized using second-order central difference schemes. Standard techniques are available for this type of discretization on arbitrary grids in textbooks and literature. For high Reynolds number flows, explicit time advancement schemes for the diffusion terms are usually acceptable, except that in the near wall region viscous effects become dominant and implicit schemes for these terms become necessary in a wall-resolved simulation. Therefore, focus for the discretization of the diffusion and source terms will be on an approach that can be used to achieve high efficiency in the implicit treatment, similar to the approximate factorization method and the consequent parallel tridiagonal linear system solver used in the orthogonal grid solvers. More discussions will be given in the following section.

The derivative with respect to the normal at the cell face is evaluated by

$$\frac{\partial u_j}{\partial n_k} = \frac{(u_j)_{nbr} - (u_j)_c}{\delta n_k}, \tag{34}$$

where δn_k is the distance between cell centers of cells c and nbr.

Velocity-Pressure Coupling Integration of Eq. (3.20) over the computational cell of volume Ω obtains,

$$\int \frac{\partial}{\partial x_j}\left(\frac{1}{\rho}\frac{\partial p^{n+1}}{\partial x_j}\right) d\Omega = \frac{1}{\Delta t}\int \frac{\partial u_j^*}{\partial x_j} d\Omega, \tag{35}$$

Applying the divergence theorem, the above equation is approximated numerically as,

$$\sum_{k=1}^{dim}\left[\frac{1}{\rho}\frac{\partial p^{n+1}}{\partial n_k} S\right]_{lf}^{uf} = \frac{1}{\Delta t}\sum_{k=1}^{dim}[U_k^*]_{lf}^{uf}, \tag{36}$$

where U_k^* is the intermediate volume flux to the cell face. The pressure Poisson equation will be solved using a semi-coarsening multigrid Poisson solver from the HYPRE library from Lawrence Livermore National Laboratory (Falgout et al., 2006). The face normal velocity can be updated by

$$U_k^{n+1} = U_k^* - \Delta t \frac{1}{\rho}\frac{\partial p^{n+1}}{\partial n_k} S, \tag{37}$$

Face-centered Velocity Components Since the Cartesian velocity components are located at the cell centers, it is necessary to reconstruct the face-centered (contra-variant) velocity components for the calculation of grid cell divergence, similar to the staggered grid configuration. For flows with constant physical properties, simple linear (using Eqs. (3.32) and (3.33)) or upwind reconstruction (Ge and Sotiropoulos, 2007) can be used to directly interpolate the cell-centered Cartesian velocity components to the face-centered locations. For two-phase flows, in order to maintain the accuracy near the interface, in (Sussman et al., 2007) more sophisticated reconstruction schemes were used on uniform Cartesian grids. The schemes will be evaluated for general structured grids. In (Sussman et al., 2007), the face centered forces (advective and viscous) are interpolated from the cell centered forces,

$$(C)_k = \left(\frac{C_c + C_{nbr}}{2}\right)_k, \tag{38}$$

and

$$(D)_k = \left(\frac{D_c + D_{nbr}}{2}\right)_k. \tag{39}$$

Then the intermediate face centered velocity, $(u_i^*)_k$, is calculated by

$$(u_i^*)_k = (u_i^n)_k + \Delta t\left[(C)_k + 2\frac{(D)_k}{\rho_c+\rho_{nbr}}\right]. \quad (40)$$

Balanced Force Treatment For two-phase flow simulations, it is very important to have a balanced force treatment for body forces like gravity and surface tension. On a staggered grid, with the ghost fluid method this requirement can be satisfied easily. However, with a hybrid variable arrangement, it is a little complicated in terms of how to update the pressure gradient at the cell center position. In (Sussman et al., 2007), the cell-centered pressure gradient was not obtained through averaging face-centered values; instead, the difference between the cell-centered and face-centered velocity components defined the cell-centered pressure gradient. The latter is consistent with the way how the face-centered velocity components were evaluated using the cell-centered components and will be used. The cell centered pressure gradient term is computed by

$$G(p^{n+1}) = G(p^n) + \frac{u_i^* - u_i^{n+1}}{\Delta t}. \quad (41)$$

Updating Cell-centered Velocity Components The velocity-pressure coupling is based on the face-centered velocity components. Therefore, after correction the face-centered velocity components will satisfy the divergence free condition. For the cell-centered velocity components, it is difficult to satisfy the divergence free condition. Zang et al. (1994) used a pressure gradient evaluated at the cell center position to correction the cell-centered velocity components,

$$u_i^{n+1} - u_i^* = -\Delta t G(p^{n+1}). \quad (42)$$

In (Sussman et al., 2007), the cell-centered velocity components are reconstructed from the face-centered velocity components instead of through correction using the cell-centered pressure gradient. The cell centered velocity is interpolated from the face center velocity as

$$(u_i^{n+1})_{cc} = \frac{(u_i^{n+1})_{lf} + (u_i^{n+1})_{uf}}{2}. \quad (43)$$

The approach in (Sussman et al., 2007) will be adopted in the general structured grid solver.

Linear System Solvers

In a CFD code, most of the CPU time is spent in linear solvers. For momentum and other scalar transport equations, implicit time advancement will result in large linear systems. If the advection terms are treated implicitly, the use of upwind schemes will produce unsymmetrical coefficient matrixes, which is much more expensive to solve than symmetrical systems. Also because of the non-linear nature of the advection terms, linearization is usually required for these terms in an implicit treatment and iterative procedures will be involved to retain numerical stability due to the strongly coupled properties of different variables, especially, all the velocity components in the momentum equations. In the general structured grid solver, the advection terms will be treated using semi-Lagrangian schemes, which are unconditionally stable and do not produce any entries into the linear system. In addition to semi-Lagrangian schemes, explicit schemes will be used for advection terms and similar benefits will be retained. Usually when the grid quality is reasonable, implicit treatment of the diffusion diagonal terms will be enough for stability consideration. The second-order spatial discretization on a general structured grid will generate nineteen-point stencil and a quite heavy matrix, compared with the seven-point stencil for Cartesian and orthogonal curvilinear grids. High-Reynolds number turbulent flows are in general advection-dominated and the diffusion (viscous) effects are only important near the wall, which need to be modeled anyway. Therefore, it is not cost-effective to solve the complete linear systems in their original forms for the momentum and other scalar equations. Approximate factorization method can be used to solve these equations in an alternating direction implicit (ADI) manner. Thus a large linear system from each of these equations reduces to three tri-diagonal systems. And the parallel tri-diagonal linear system solver implemented in the orthogonal grid solvers can be applied in a straightforward manner.

For other cases, iterative procedures have to be considered for stability, efficiency, and accuracy. For instance, if a grid is non-smooth and/or non-orthogonal, the off-diagonal terms may become dominant and the explicit evaluation discussed above may become unstable. On the other hand, for locally refined grids and/or overset grids, iterative methods have to be used as the parallel ADI method can only be applied to block-structured grids with matched grid interfaces. In general, the Newton-Raphson method can be used to iteratively update the whole field until convergence is reached.

A major difference for the pressure Poisson equations from the orthogonal grids and the general structured grids is the size of stencils, which increases from seven to nineteen due to the grid non-orthogonality. Therefore, the memory usage of the general grid solver will be much increased too.

The Hypre package already has the conceptual interfaces for block-structured grids, locally refined grids, and overset grids. Thus the extension of the pressure Poisson solver from orthogonal grids to general structured grids will be quite straightforward.

Overall Solution Procedure

The overall solution procedure to solve the governing equations is summarized below:

- Update the interface position by solving the VOF Eq. (15).
- Calculate cell centered convective terms and cell centered viscous terms using semi-implicit scheme. Solve Eq. (31) for the intermediate velocity $\hat{u}_i$ and Eq. (19) for velocity component u_i^*.
- Reconstruct face-centered velocity by interpolation from the cell centered velocity directly. For two-phase flows, interpolate the cell centered convective and viscous terms to cell face centers first, and then calculate $(u_i^*)_k$ using Equation (40).
- Solve pressure projection equation and correct the contra-variant velocity U_k^{n+1} through Eqs. (36) and (37).
- Interpolate face centered velocity to cell centered velocity $\left(u_i^{n+1}\right)_{cc}$ using Eq. (43).
- Update the cell centered pressure gradient terms using Eq. (41).

GRID STRUCTURE AND HPC

The distinguishing difference between the orthogonal grid solver and the general structured grid solver will be in the use of a multi-block grid structure in the latter version. The latter represents a great leap forward in that structured multi-block meshes will be adopted for greater flexibility in handling complicated geometries. Multi-block here means that the block topology can be made from multiply-connected blocks, thereby providing flexibility in representing complicated geometries which cannot be otherwise represented adequately by a single block. The general structured grid solver is highly parallelized and will be run on massively parallel supercomputers to speed up the execution time.

Structured grid generation requires a lot of human inputs and usually is the most time-consuming part in a simulation in terms of human hours. The situation is aggravated with a multi-block grid structure as connectivity between the blocks has to be taken into account as well. To this end, the original rudimentary input data format adopted in the orthogonal grid solvers (Plot3D) will be replaced by the more sophisticated and versatile CGNS (CFD General Notation System) data format. The CGNS system is designed to facilitate the exchange of data between sites and applications, and to help stabilize the archiving of data. The data are stored in a compact, binary format and are accessible through an extensive and extensible library of functions. Though the CGNS format confronts the modeler with a much steeper learning curve with its complexity and multitude of available options, it offers several advantages over the Plot3D format which justify its adoption in the general structured grid solver. To enumerate, its principal capabilities include: a) Structured, unstructured, and hybrid grids; b) Flow solution data, which may be nodal, cell-centered, face-centered, or edge-centered; c) Multi-block interface connectivity including both abutting and overset types; d) Boundary conditions; e) Dimensional units and non-dimensionalization information.

With the above advantages, it is conceivable the CGNS format will offer us with greater control over the multi-block data structure; enabling us to concentrate on the implementation of the MPI decomposition rather than diverting our attention toward the multi-block interface connectivity which can be a painful and time-consuming task. Further, since boundary conditions are already included in the input CGNS data, much time is saved implementing the boundary conditions for individual blocks in the FORTRAN code. For complicated geometries, the mesh generation can be done with the commercial software POINTWISE which is able to output the mesh data conveniently in CGNS format along with the boundary conditions and grid connectivity. Finally, since CGNS supports overset grids, its adoption facilitates future extensions of the general structured grid solver to include overset grid capability.

The existing grid topology in the orthogonal grid solvers for a single block is no longer applicable and will be completely overhauled by a more sophisticated grid topology which is capable of handling a multi-block structure and which takes advantage of the new capabilities of the CGNS data format. For instance, CGNS format can handle grid block connectivity and ghost cell mapping information naturally. The need to map ghost cell data from one processor to another is due to the nature of the finite extent of the FE/FV stencil which typically extends over neighboring cells. If the neighboring cells reside in a different MPI domain, information then needs to be communicated across different MPI processors.

RESULTS

Plunging Wave Breaking Behind a Bump

Plunging wave breaking is of great importance to ship hydrodynamics, including strong turbulence with large amounts of air bubbles, water droplets, jets, and sprays. Previous experimental fluid dynamics (EFD)

and CFD studies on plunging wave breaking are mainly focused on the global structures of the wave breaking, such as wave elevation, jet, air entrainment, etc. Moreover, due to the technical difficulties, the experimental measurements can only be done in the water region, and detailed description of the energetic wave breaking region is not available. With the development of the CFD technology, detailed studies of the two-phase region are possible. In order to resolve the small structures of the wave breaking, such as air bubbles and water droplets at the scale of several micrometers, large scale parallel computations (several billion grid points) are needed.

In the present study, plunging wave breaking generated by an impulsive flow over a submerged bump is simulated with a focus on the small scale features such as the spray formation, air bubble size and distribution, and 3D vortex structures. In the study by Wang et al. (2009a), simulations were conducted on a 2D domain using an immersed boundary method on Cartesian grids. The experimental study with detailed flow conditions and the corresponding computational study are presented in Koo et al. (2012) and Kang et al. (2012), respectively. In the present study, a 3D LES of the impulsive plunging wave breaking is performed on an orthogonal curvilinear grid using CFDShip-Iowa Version 6.2 (Suh et al., 2011).

3D simulations of the impulsive plunging wave breaking are performed on orthogonal curvilinear grids with some preliminary results reported. The computational domain and boundary conditions are shown in Koo et al. (2012). The constant inlet velocity imposed at the left boundary is u = 0.87m/s for water and zero for air. The initial interface elevation is 0.2286m and a uniform velocity field is prescribed in the water domain with the air phase at rest. The computational results with a grid of 768 × 256 × 64 are compared with the experimental video images in Figure 2. The major events of the first plunge wave breaking are demonstrated, i.e., maximum height, first plunge, oblique splash, and vertical jet as identified by Wang et al. (2009a) using 2D simulations. On the video images, the entrapped air tube is marked by a circle. As shown in the figure, the computational results match the experiments very well.

For droplet and bubble size distribution, three grids of dimension 1920×1280×896 (2.2 Billion), 960×640×448, and 480×320×224 have been used. The results computed on the fine grid of 1920×1280×896 are presented in Figure 3 which shows bubble and droplet formation. Figure 3(a) shows the jet plunging on the water surface with entrapped air cavity. The air cavity collapses and breaks up into air bubbles as shown in Figure 3(b). Various sizes of droplets generated in the splash-up region are shown in Figure 3(c). The experimental study (Deane and Stokes, 2002) shows that two distinct flow conditions that drive bubble creation in breaking waves: jet plunging and collapse of the cavity. The bubble sizes are from 2 mm down to at least 0.1 mm for the jet plunging period, larger bubbles from 2 mm to $\geq$ 10 mm are created due to the collapse of the cavity. For the fine grid 1920×1280×896, the average grid spacing in the wave breaking region is 0.25 mm, which can effectively capture most bubbles with the sizes reported in the experiments. The simulation on the fine grid is still underway which will be discussed in future studies. The bubble and droplet size distribution based on the fine grid simulation will also be investigated in future studies.

Interface-Piercing Circular Cylinder

Large-eddy simulation of the flow past a surface-piercing circular cylinder has been performed for critical Reynolds (Re) and Froude (Fr) numbers, and compared with the previous study based on the experiments of Chaplin and Teigen (2003). In this study, Reynolds number effect on flow structures near the interface was investigated for three different Reynolds numbers from sub-critical to critical ($Re = 2.7 \times 10^4, 2.34 \times 10^5, 4.58 \times 10^5$) with constant $Fr = 0.84$. Froude number effect on flow structures was investigated for $Re = 4.58 \times 10^5$ in terms of air-water interface structures, vorticity and velocity at the interface and wave breaking.

Three different Re from sub-critical to critical ($Re = 2.7 \times 10^4, 2.34 \times 10^5, 4.58 \times 10^5$) with the same $Fr = 0.84$ are used to investigate Re effect on flow structure near the interface. The separation pattern of the mean flow with vortex core lines is shown in Figure 4. The separated region at the interface decreases as Re increases from sub to critical since the separation point is delayed. Immediately below the interface, the separation region is reduced for all Re and "neck" shape is observed especially. It is noticeable that for $Re = 4.58 \times 10^5$, the separated region is detached from the cylinder wall in deep water probably due to the separation bubble. In higher Re, the separation point is much delayed and the narrowing of the wake is observed from the critical Re ($2.34 \times 10^5, 4.58 \times 10^5$) and the separation point moves downstream as with Re increase.

The Fr number effect is studied using the case with $Re = 4.58 \times 10^5$. Figure 5 presents the close-up view of the mean air-water interface elevation contours with iso-surface near the cylinder. Contour levels for high Fr (1.64) is 2 and about 5 times greater than those for medium (1.24) and low Fr (0.84), respectively. For

$Fr = 0.84$, the Kelvin waves propagate with a wide angle and relatively small depression depth behind the cylinder. For $Fr = 1.24$, the depression region immediately behind the cylinder is narrow and deep, which makes the cylinder act like a slender body, and this causes smaller diverging angle than that of low Fr. For $Fr = 1.64$, much larger depression depth is observed, and it is even narrower and longer than that of both low and medium Fr, implying that the flow past the cylinder at $Fr = 1.64$ shows features with more slender body.

Three-dimensional instantaneous coherent vertical structures for three Fr are shown in Figure 6. The results for Fr of 0.84 are consistent with the previous work (Suh et al., 2011). Due to the interface deformation, smaller scale of vertical structures are observed at the air-water interface for all three Fr. Especially, at medium and high Fr, small vertical structures near the interface are disappeared due to the cavity region behind the cylinder and there are only large structures in the deep flow.

Interface-Piercing Circular Cylinder with a Pure Sway Motion

A periodically oscillating surface-piercing circular cylinder in a free-stream is considered. Two non-dimensional parameters are also involved so as to characterize the flow induced by the periodic motion of the cylinder. Besides the Reynolds number, the Keulegan-Carpenter number is defined as $KC = U_{\max}/fD$, where $U_{\max}$ is the maximum velocity of the cylinder, and f is the frequency of the oscillation.

Fig. 7 shows the computational domain and coordinate system. The grid is $128 \times 256 \times 128$. In this calculation, the cylinder is in two-phase flow (air and water), only water comes into the cylinder in an inertial reference frame as initial and boundary conditions. The direction of the motion is perpendicular to the free stream, i.e., $Z_c = -A\cos(2\pi ft)$, with Z_c the position of the center of the cylinder and A the amplitude of the oscillation. The test is calculated at $Re = 2.7 \times 10^4$ and the amplitude of motion is set to $A/D = 0.2$. The frequency of the motion is assumed to be the same as the Strouhal number of a circular cylinder in uniform single-phase flow ($St = 0.5$). Dirichlet boundary conditions are used for inlet and all outer boundaries, and convective boundary conditions are applied at outlet.

Some preliminary results have been obtained. Fig. 8 shows the free-surface elevation contours at several different phase angles. The deviated wake due to the sway motion of the cylinder is evident.

CONCLUSIONS

In this paper, the motivation and objectives of developing a high-fidelity multi-block general structured grid two-phase flow solver for ship hydrodynamics have been presented first. In order to demonstrate the feasibility of such a solver for complicated multi-phase, multi-physics, and multi-scale naval hydrodynamics problems, an orthogonal curvilinear grid solver capable of billion-point simulations developed recently has been summarized. The mathematical formulation for high-fidelity LES of two-phase incompressible flows has been given and the detailed numerical methods for the general structured grid solver have been presented.

Some recent applications performed using the orthogonal curvilinear grid solver have been demonstrated. High-resolution simulations of the plunging breaking waves behind a bottom-mounted bump in a shallow water flume have been performed using three different grids. The fine grid has 2.2 billion grid points, which can resolve many small droplets and bubbles. This will be a major step toward obtaining droplet/bubble size distribution in a numerical simulation. In this paper, some preliminary results from the fine grid have been given. The computed breaking waves agree with images obtained from the flume experiments very well. The high-Re/Fr free-surface flow past an interface-piercing circular cylinder has been studied. The effects of Reynolds and Froude numbers have been discussed. Some preliminary results from an interface-piercing circular cylinder with a periodic sway motion have been presented too. Further discussions on the plunging wave breaking behind the bump and the interface-piercing cylinder cases will be discussed elsewhere.

Currently the general structured grid solver is still under development and testing. In our future work, verification and validation cases for both single phase cases and two-phase cases will be studied to demonstrate the accuracy of the solver. The Wigley hull case will also be solved to show its capability in handling non-orthogonal curvilinear grids common in computational ship hydrodynamics.

ACKNOWLEDGMENTS

This research was sponsored by the Office of Naval Research under Grant N000141-01-00-1-7, under the administration of Dr. Patrick Purtell. Dr. K.W. Cheng is acknowledged for the initial version of section “Grid Structure and HPC.”

REFERENCES

Bhushan, S., Hanaoka, A., Yang, J., and Stern, F., "Wall-Layer Modeling for Cartesian Grid Solver Using an Overset Boundary Layer Orthogonal Curvilinear Grid," AIAA-2011-0756, Proceedings of the 49th AIAA Aerospace Sciences Meeting and Exhibit, 4-7 January 2011b, Orlando, Florida.

Carrica, P.M., Wilson, R.V., Noack, R.W., and Stern, F., "Ship Motions Using Single-Phase Level Set with Dynamic Overset Grids," Computers & Fluids, Vol. 36, 2007, pp. 1415-1433.

Choi, H., and Moin, P., "Effects of the Computational Time Step on Numerical Solutions of Turbulent Flow," Journal of Computational Physics, Vol. 113, 1994, pp. 1-4.

Falgout, R.D., Jones, J.E., and Yang, U.M., "The Design and Implementation of HYPRE, Library of Parallel High Performance Preconditioners," Numerical Solution of Partial Differential Equations on Parallel Computers. A.M. Bruaset and A. Tveito, eds. Springer-Verlag. Vol. 51, 2006, pp. 267-294.

Ge, L. and Sotiropoulos, F., "A Numerical Method for Solving the 3D Unsteady Incompressible Navier–Stokes Equations in Curvilinear Domains with Complex Immersed Boundaries," Journal of Computational Physics, Vol. 225, 2007, pp. 1782-1809.

He, P., Salcudean, M., Gartshore, I.S., and Nowak, P., "Multigrid Calculation of Fluid Flows in Complex 3D Geometries Using Curvilinear Grids," Computers & Fluids, Vol. 25, 1996, pp. 395-419.

Kang, D., Ghosh, S., Reins, G., Koo, B., Wang, Z., and Stern, F., "Impulsive Plunging Wave Breaking Downstream of a Bump in a Shallow Water Flume — Part I: Experimental Observations," Journal of Fluids and Structures, in press, 2012.

Koo, B., Wang, Z., Yang, J., and Stern, F., "Impulsive Plunging Wave Breaking Downstream of a Bump in a Shallow Water Flume —Part II: Numerical Simulations," Journal of Fluids and Structures, in press, 2012.

Meneveau, C., Lund, C.S., and Cabot, W.H., "A Lagrangian Dynamic Subgrid-scale Model of Turbulence," Journal of Fluid Mechanics, Vol. 319, 1996, pp. 353-385.

Shyy, W., Vu, T.C., "On the Aadoption of Velocity Variable and Grid System for Fluid Flow Computation in Curvilinear Coordinates," Journal of Computational Physics, Vol. 92, 1991, pp. 82-105.

Smith, K.M., Cope, W.K., and Vanka, S.P., "A Multigrid Procedure for Three-dimensional Flows on Non-orthogonal Collocated Grids," International Journal for Numerical Methods in Fluids, Vol. 17, 1993, pp. 887-904.

Suh, J., Yang, J. and Stern, F., "The Effect of Air-Water Interface on the Vortex Shedding from a Vertical Circular Cylinder," Journal of Fluids and Structures, Vol. 27, 2011, pp. 1-22.

Sussman, M., Smith, K.M., Hussaini, M.Y., Ohta, M., and Zhi-Wei, R., "A Sharp Interface Method for Incompressible Two-Phase Flows," Journal of Computational Physics, Vol. 221, 2007, pp. 469-505.

Wang, Z., Yang, J., and Stern, F., "An Improved Particle Correction Procedure for the Particle Level Set Method," Journal of Computational Physics, Vol. 228, 2009a, pp. 5819-5837.

Wang, Z., Yang, J., Koo, B. and Stern, F., "A Coupled Level Set and Volume-Of-Fluid Method for Sharp Interface Simulation of Plunging Breaking Waves," International Journal of Multiphase Flow, Vol. 35, 2009b, pp. 227-246.

Wang, Z., Yang, J., Stern, F., "A New Volume-Of-Fluid Method with a Constructed Distance Function on General Structured Grids," Journal of Computational Physics, Vol. 231, 2012a, pp. 3703-3722.

Wang, Z., Yang, J., and Stern, F., "A Simple and Conservative Operator-Splitting Semi-Lagrangian Volume-Of-Fluid Advection Scheme," Journal of Computational Physics, Vol. 231, 2012b, pp. 4981-4992.

Wang, Z., Suh, J., Yang, J., and Stern, F., "Sharp Interface LES of Breaking Waves by an Interface Piercing Body in Orthogonal Curvilinear Coordinates," AIAA-2012-1111, Proceedings of the 50th AIAA Aerospace Sciences Meeting and Exhibit, 2012c, Nashville, Tennessee.

Wesseling, P., Segal, A., and Kassels, C.G.M., "Computing Flows on General Three-Dimensional Nonsmooth Staggered Grids," Journal of Computational Physics, Vo. 149, 1999, pp. 333-362.

Yang, J., Bhushan, S., Suh, J., Wang, Z., Koo, B., Sakamoto, N., Xing, T., and Stern, F., "Large-Eddy Simulation of Ship Flows with Wall-layer Models on Cartesian Grids," Proceedings of the 27th Symposium on Naval Hydrodynamics, Seoul, Korea, 2008b.

Yang, J., and Stern, F., "Sharp Interface Immersed-Boundary/Level-Set Method for Wave-Body Interactions," Journal of Computational Physics, Vol. 228, 2009, pp. 6590-6616.

Yang, J., and Stern, F., "A Simple and Efficient Direct Forcing Immersed Boundary Framework for Fluid-Structure Interactions," Journal of Computational Physics, Vol. 231 2012, pp. 5029-5061.

Zang, Y., Street, R.L., and Koseff, R., "A Non-Staggered Grid, Fractional Step Method for Time-Dependent Incompressible Navier-Stokes Equations in

Curvilinear Coordinates," Journal of Computational Physics, Vol. 114, 1994, pp. 18-33.

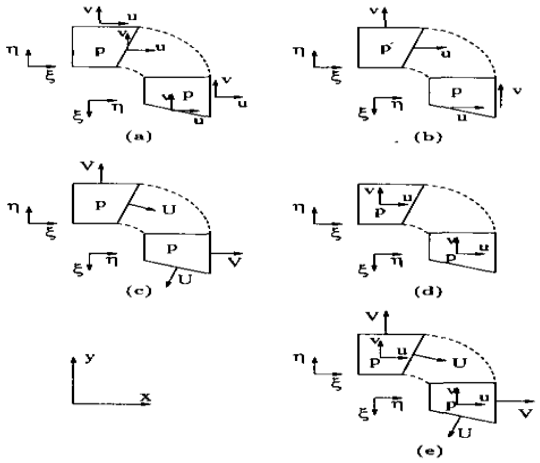

Figure 1. Grid layouts and dependent variables (Zang et al., 1994).

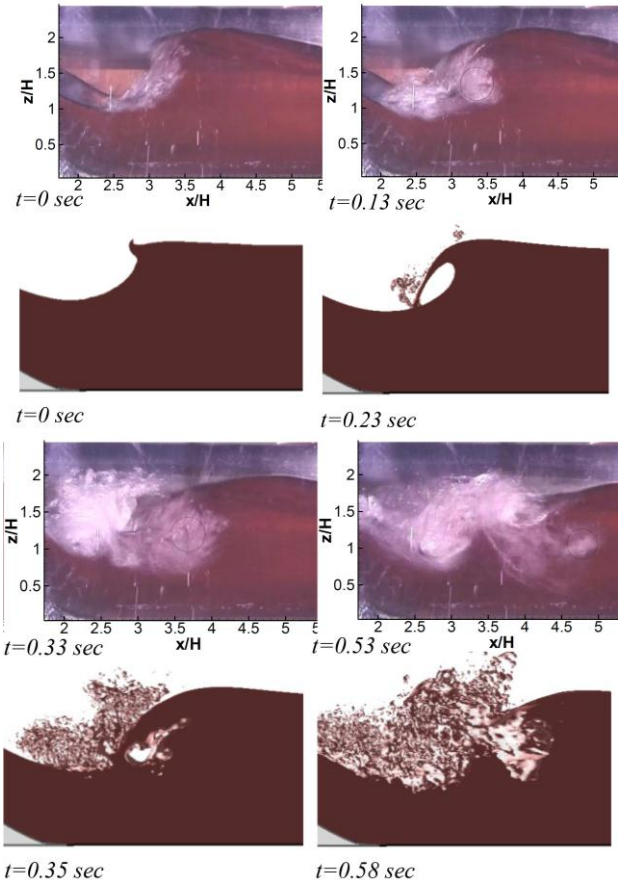

Figure 2. Wave breaking process behind a submerged bump. Top: EFD; bottom: CFD.

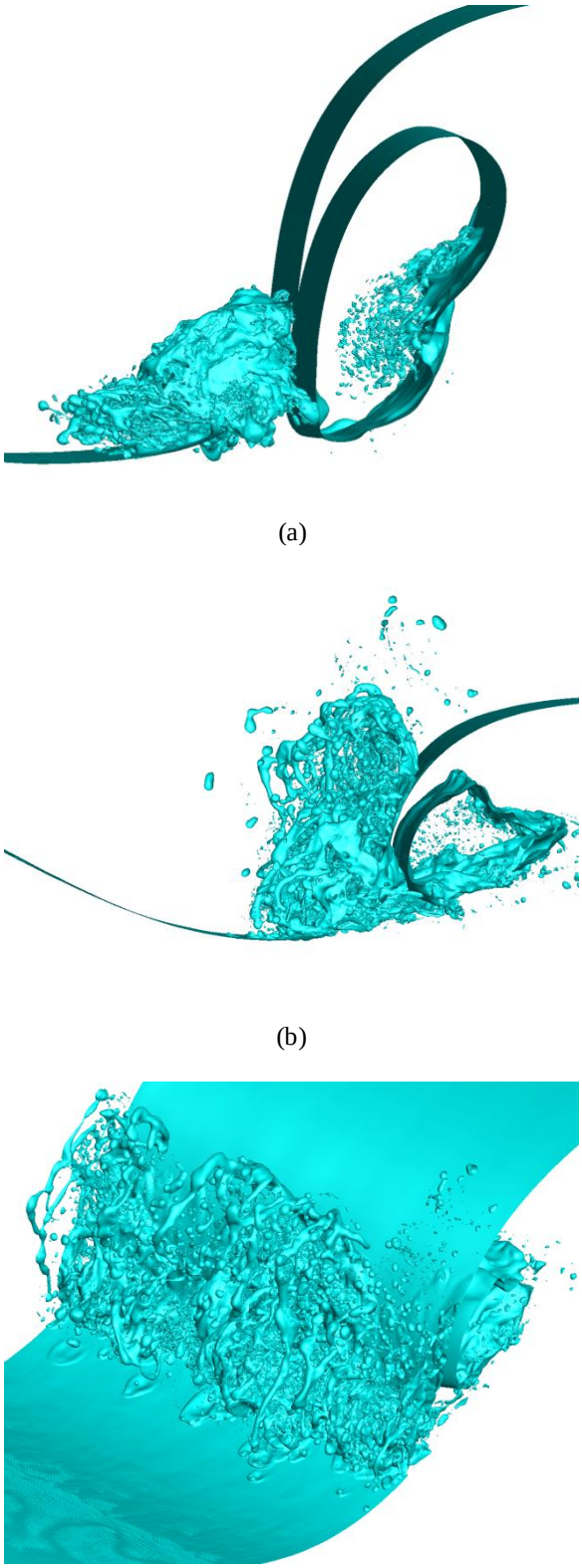

(a)

(b)

(c)

Figure 3 Droplets and bubble formation of the wave breaking over a submerged bump. Grid: 960×640×448. (a). Jet plunging; (b). cavity collapsing. (c). oblique view.

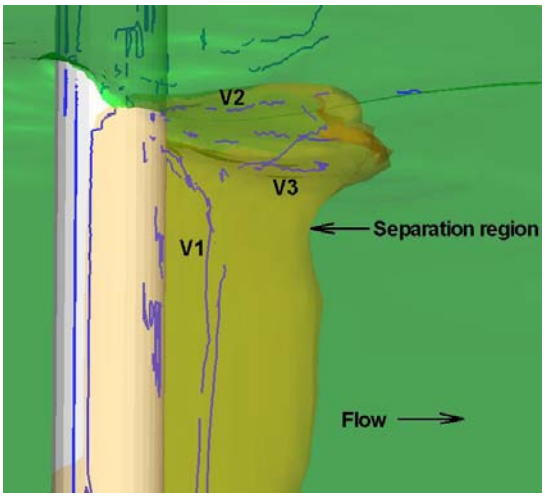

(a)

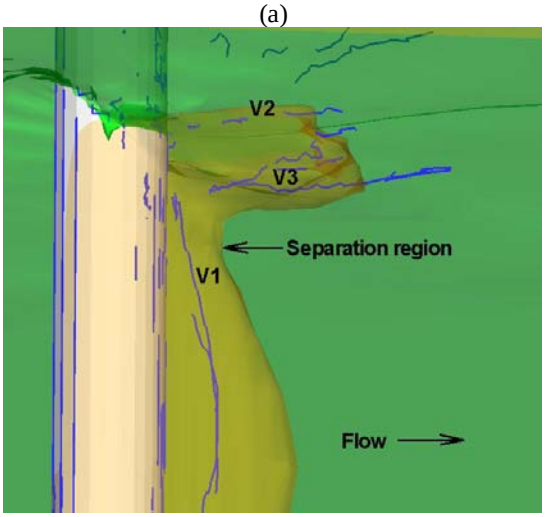

(b)

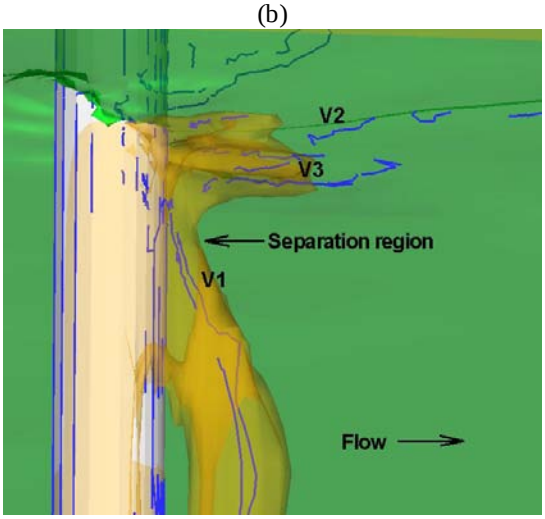

(c)

Figure 4. Mean separation pattern with vortex core lines: (a) Re = 27,000; (b) Re = 234,000; (c) Re = 458,000.

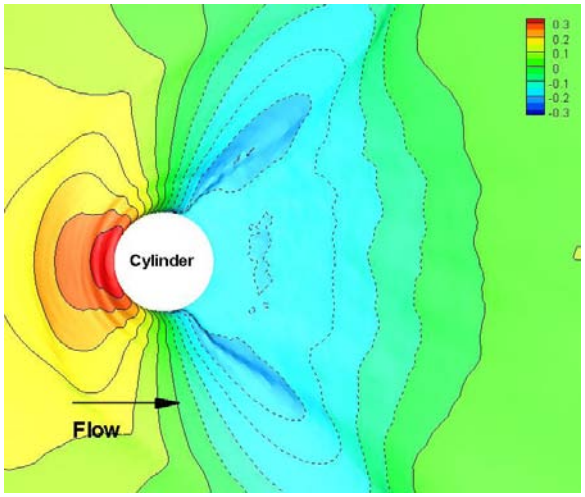

(a)

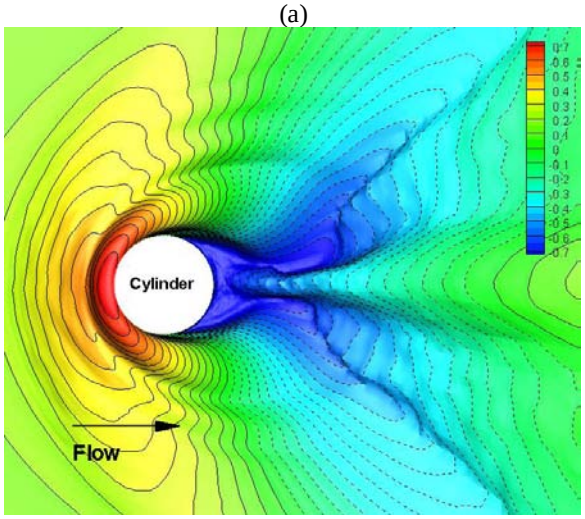

(b)

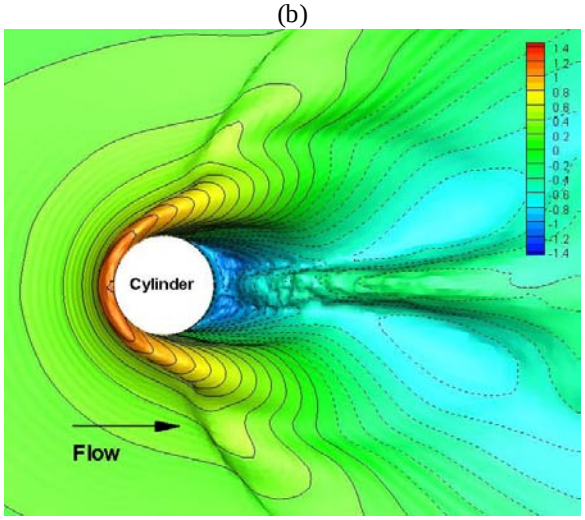

(c)

Figure 5. Close-up of mean air-water interface elevation contours: (a) Fr=0.84; (b) Fr=1.24; (c) Fr=1.64.

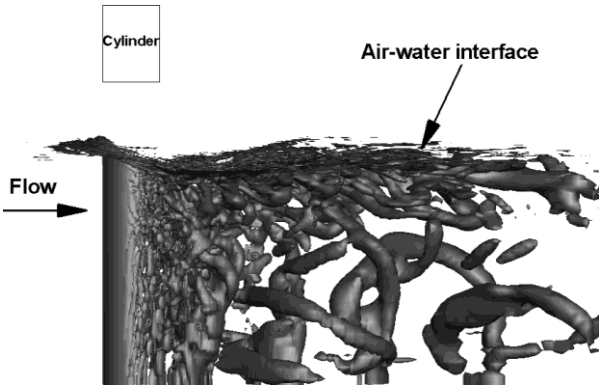

(a)

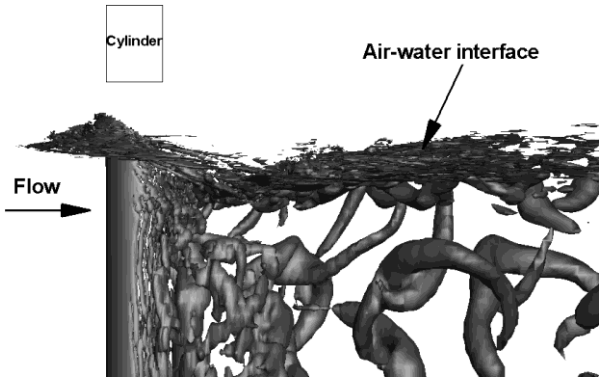

(b)

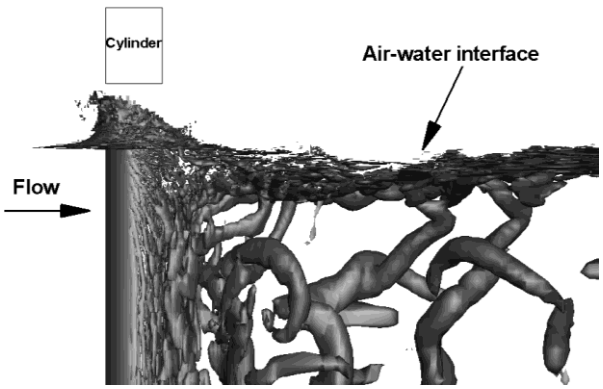

(c)

Figure 6. Instantaneous vortical structures identified by the second invariant of the velocity gradient tensor Q = 1.0 for three Fr : (a) Fr=0.84; (b) Fr=1.24; (c) Fr=1.64.

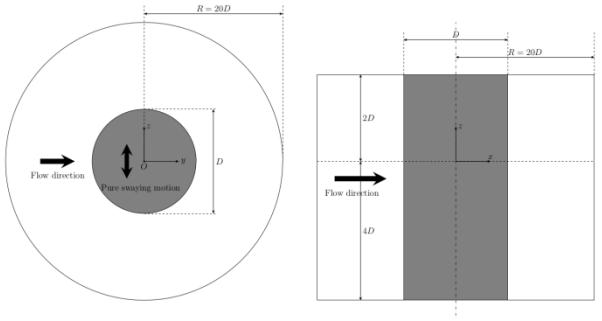

(a) (b)

Figure 7. Schematic diagram of the computational domain and coordinate system.

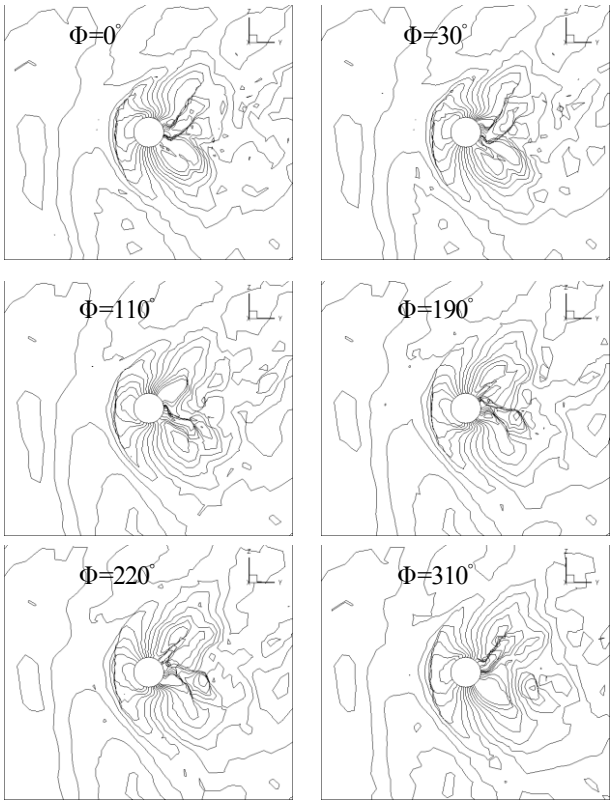

Figure 8. Freesurface elevation contour at various phase angle Φ= 0, 30, 110, 190, 220, 310◦.